

THE SUBSTRUCTURES IN THE LOCAL STELLAR HALO FROM GAIA AND LAMOST

HEFAN LI¹, CUIHUA DU^{2,3}, SHUAI LIU⁴, THOMAS DONLON³, HEIDI JO NEWBERG³

¹School of Physical Sciences, University of Chinese Academy of Sciences, Beijing 100049, P. R. China;

²College of Astronomy and Space Sciences, University of Chinese Academy of Sciences, Beijing 100049, China; ducuihua@ucas.ac.cn

³Department of Physics, Applied Physics and Astronomy, Rensselaer Polytechnic Institute, Troy, NY 12180, USA

⁴Key Laboratory of Optical Astronomy, National Astronomical Observatories, Chinese Academy of Sciences, Beijing 100012, China

Draft version February 14, 2019

ABSTRACT

Based on the second Gaia data release (Gaia DR2) and spectroscopy from the Large Sky Area Multi-Object Fiber Spectroscopic Telescope (LAMOST) Data, we identified 20,089 halo stars kinematically and chemically. The halo streams in the solar neighborhood could be detected in the space of energy and angular momentum. We reshuffle the velocities of these stars to determine the significance of substructure. Finally, we identify 4 statistically significant substructures that are labeled GL-1 through 4. Among these substructures, GL-1 is previously known stream (“N2” stream) and the rest 3 substructures are new. These substructures may be the debris of dwarf galaxies accretion event, their dynamical and chemical information can help to understand the history of the Milky Way.

Subject headings: Galaxy: kinematics and dynamics - Galaxy: halo - Solar neighborhood

1. INTRODUCTION

In the standard hierarchical model of galaxy formation, stellar halos are thought to form via the accumulation of stars from dwarf galaxies that accreted and merged with a larger galaxy. This merging process left behind many stellar streams or moving groups in the Galactic halo (Searle & Zinn 1978; Freeman & Bland-Hawthorn 2002). Although the accumulated debris from old accretion events rapidly disperses in real space, stellar halos still maintain visible fossil structure in their phase space distribution (Helmi & White 1999a; Bullock & Johnston 2005). Nonetheless, many Galactic halo substructures have been spatially identified using data from large sky surveys such as the Sloan Digital Sky Survey (SDSS; York et al. 2000), Hipparcos (van Leeuwen 2007), the Radial Velocity Experiment (RAVE; Steinmetz et al. 2006), the Two Micron All-Sky Survey (2MASS; Skrutskie et al. 1997) and Wide-Field Infrared Survey Explorer (WISE; Wright et al. 2010) surveys. Some of the substructures identified include: the Sagittarius dwarf tidal stream (Ibata et al. 1994; Majewskia et al. 2003; Belokurov et al. 2006), the Orphan Stream (Grillmair 2006; Belokurov et al. 2007; Newberg et al. 2010) and the Virgo Stellar Stream (Duffau et al. 2006; Newberg et al. 2007; Duffau et al. 2014). Grillmair & Carlin (2016) summarize the methods used for discovering streams and present tables that give some basic information for most of the streams and clouds found before 2015, and they also discuss the properties of individual tidal debris structures.

Numerical simulations predict that most accreted satellites would also spread their tidal debris into the Galactic inner halo (Helmi & White 1999a) or even the disk component (Abadi et al. 2003), thus we can expect to find debris remnants in the local halo. Some efforts have been made to find the debris relics in the local halo and the observational evidence is slowly growing. For example, Helmi et al. (1999b) have detected two streams in the solar neighborhood by studying the angular momentum of stellar orbits. Smith et al. (2009) found four discrete overdensities localized in angular momentum in the solar neighborhood and suggested that they may be possible accretion remnants. Kepley et al. (2007) assem-

bled a sample of halo stars in the solar neighborhood to find two new halo substructure in velocity and angular momentum space. Morrison et al. (2009) have also shown that the angular momentum distribution of a sample of stars does not seem to be smooth, possibly indicative of an accretion origin. Klement (2010) summarizes the discoveries of solar neighborhood stellar halo streams and gives a theoretical overview over the search strategies employed. Recently, Helmi et al. (2017) study the distribution of local halo stars in “Integrals of Motion” space using the TGAS dataset, in combination with data from the RAVE survey and discover several substructures that could potentially be related to merger events. Although no longer spatially coherent, such stellar streams keep their common origin imprinted into their chemical and dynamical properties. This allows us constrain various scenarios of hierarchical buildup of the Galaxy (e.g., Helmi & White 1999a) from the phase-space distribution of local halo stars.

The chemical evolution of stellar halos (Tissera et al. 2014), supports the idea that the outer halo formed primarily through the accretion of smaller stellar systems like dwarf spheroidal (dSph) galaxies (Searle & Zinn 1978; Sales et al. 2007; Diemand et al. 2008; Springel et al. 2008; Klypin et al. 2011). On the other hand, part of the inner halo may have formed in-situ, either from dissipative collapse of gaseous material onto the central region of the Galaxy (Eggen et al. 1962; Zolotov et al. 2010; Font et al. 2011), or from a heated disk during merger events (Cooper et al. 2015). Evidence for the dual halo (either inner vs. outer, or metal-rich vs. metal-poor) has been found from the kinematics of stars near the Sun by Chiba & Beers (2000); Carollo et al. (2007, 2010); Deason et al. (2017); Belokurov et al. (2018). It is possible that the inner-halo was also built by accretion.

Thanks to modern sky surveys that provide radial velocities and proper motions, we can use the full 6D phase space information for halo stars to search for substructures in the solar neighborhood. This will allow us to search for older substructures that could have lost their spatial coherence but maintain coherence in energy and angular momentum.

ESA’s Gaia mission has produced the richest star catalogue

to date, including high-precision measurements of nearly 1.7 billion stars (Gaia Collaboration 2018), in April 2018. Gaia DR2 included positions, distance indicators and motions of more than one billion stars. To obtain the required full phase-space information of halo stars, we also use radial velocities and metallicities derived from Large Sky Area Multi-Object Fiber Spectroscopic Telescope (LAMOST; Cui et al. 2012; Deng et al. 2012; Zhao et al. 2012). In July 2017, LAMOST release its the Data 5 (LAMOST DR5), which includes over 9 million spectra. In this paper, we will use the combined data set obtained by cross-matching Gaia to LAMOST to find the potential substructures.

The paper is organized as follows. In Section 2, we introduces the observational data from Gaia and LAMOST, describe the sample selection, and define the coordinate systems used in this study. The detection strategy and analysis of detected substructures are discussed in Section 3. The conclusions are summarized in Section 4.

2. DATA

2.1. *Gaia and LAMOST*

The Gaia satellite is a space-based mission launched at the end of 2013 and started science operations the following year. The second Gaia data release (Gaia DR2) includes high-precision measurements of nearly 1.7 billion stars (Gaia Collaboration 2018). As well as positions, the data include astrometry, photometry, radial velocities, and information on astrophysical parameters and variability, for sources brighter than magnitude 21. This data set contains positions, parallaxes, and mean proper motions for about 1.3 billion of the brightest stars. For a subset of stars within a few thousand parsec of the Sun, Gaia has measured the velocity in all three dimensions.

The Large Sky Area Multi-Object Fiber Spectroscopic Telescope (LAMOST, also called the Guo Shou Jing Telescope) is a 4 meter quasi-meridian reflective Schmidt telescope with 4000 fibers within a field of view of 5° . The LAMOST spectrograph has a resolution of $R \sim 1,800$ and wavelength range spanning 3,700 Å to 9,000 Å (Cui et al. 2012). LAMOST has completed 5 years of survey operations plus a Pilot Survey, and has internally released over 9 million spectra to the collaboration. The survey reaches a limiting magnitude of $r = 17.8$ (where r denotes magnitude in the SDSS r -band), but most targets are brighter than $r \sim 17$. The LAMOST Stellar Parameter Pipeline (Wu et al. 2011; Luo et al. 2015) estimates parameters, including radial velocity, effective temperature, surface gravity and metallicity ([Fe/H]) from LAMOST spectra. The accuracy depends on wavelength calibration, spectral type and SNR of spectra. The accuracies in measuring radial velocity and [Fe/H] at $R = 1800$ are expected to be 7 km s^{-1} and 0.1 dex, respectively (Zhao et al. 2012). In total, there are over 5 million stars in the A, F, G and K type star catalog.

The estimated systematic offset of Gaia DR2 parallaxes is -0.029 based on quasar (Lindegren et al. 2018). Using the catalogue of radial velocity standard stars provided by Huang et al. (2018), we determine the radial velocity zero-points (RVZPs) of LAMOST DR5 is $\Delta RV = -4.70 \text{ kms}^{-1}$. The parallax and radial velocity measurements are corrected with their offsets in the following study. Our initial sample was obtained by cross-matching between the Gaia and LAMOST catalogs, based on stellar position. After imposing the requirements that relative parallax error $\leq 20\%$, the signal-to-

noise ration (SNR) ≥ 20 and radial velocity error $\epsilon_{RV} \leq 10 \text{ km s}^{-1}$, the data set contains 2,641,631 stars.

2.2. Coordinate transformations

To get full 6D phase-space information, we transform the coordinates measured for the stars into a Cartesian coordinate system.

Parallaxes are one of the few distance measures in astronomy which do not require assumptions about the intrinsic properties of the object. Despite the simple relation between the parallax and distance, inversion of the parallax to obtain distance is only appropriate when there are no measurement errors. So we use the full Bayesian approach to infer distances and velocities (Luri et al. 2018). We use the exponentially decreasing space density prior in distance d (Bailer-Jones et al. 2018):

$$P(d | L) \propto d^2 \exp(-d/L) \quad (1)$$

and assume that the prior of v_α, v_δ, v_r are uniform. Then we can write the posterior as:

$$P(\theta | x) \propto \exp[-\frac{1}{2}(x - m(\theta))^T C_x^{-1} (x - m(\theta))] P(d | L) \quad (2)$$

where $\theta = (d, v_\alpha, v_\delta, v_r)^T$, $x = (\varpi, \mu_\alpha^*, \mu_\delta, rv)^T$, $m = (1/d, v_\alpha/kd, v_\delta/kd, v_r)^T$, $k = 4.74$ and C_x^{-1} is covariance matrix. We choose the most probable value of $d, v_\alpha, v_\delta, v_r$ in the posterior as the estimator of the distances and velocities.

We calculate the Galactocentric Cartesian (x, y, z) coordinates (Jurić et al. 2008) from the Galactic (l, b) coordinates and distances as follows:

$$\begin{aligned} x &= R_\odot - d \cos(b) \cos(l) \\ y &= -d \cos(b) \sin(l) \\ z &= d \sin(b) + z_\odot \end{aligned} \quad (3)$$

where $R_\odot = 8.2 \text{ kpc}$ is the distance to the Galactic center (Bland-Hawthorn & Gerhard 2016), $z_\odot = 25 \text{ pc}$ is the solar offset from local disk midplane (Jurić et al. 2008), d is distance of the star from the Sun, and (l, b) are the Galactic coordinates. We calculate each star's Galactic space-velocity components, U, V and W , from its $d, v_\alpha, v_\delta, v_r$ mentioned above (Johnson & Soderblom 1987). We correct for the solar peculiar motion of $(U, V, W) = (10., 11., 7.) \text{ km s}^{-1}$ (Tian et al. 2015; Bland-Hawthorn & Gerhard 2016) relative to the local standard of rest (LSR). Here, we assume that the LSR velocity is $V_{\text{LSR}} = 232.8 \text{ km s}^{-1}$ in the direction of rotation (McMillan 2017).

We calculate the cylindrical velocities:

$$\begin{aligned} v_R &= -U \cos(\phi) - V \sin(\phi) \\ v_\phi &= U \sin(\phi) - V \cos(\phi) \\ v_z &= -W \end{aligned} \quad (4)$$

where $\phi = \tan^{-1}(y/x)$, and the spherical velocities for our sample:

$$\begin{aligned} v_r &= -U \sin(\theta) \cos(\phi) - V \sin(\theta) \sin(\phi) - W \cos(\theta) \\ v_\theta &= -U \cos(\theta) \cos(\phi) - V \cos(\theta) \sin(\phi) + W \sin(\theta) \\ v_\phi &= U \sin(\phi) - V \cos(\phi) \end{aligned} \quad (5)$$

where $r = \sqrt{x^2 + y^2 + z^2}$, $\theta = \cos^{-1}(z/r)$ and $\phi = \tan^{-1}(y/x)$.

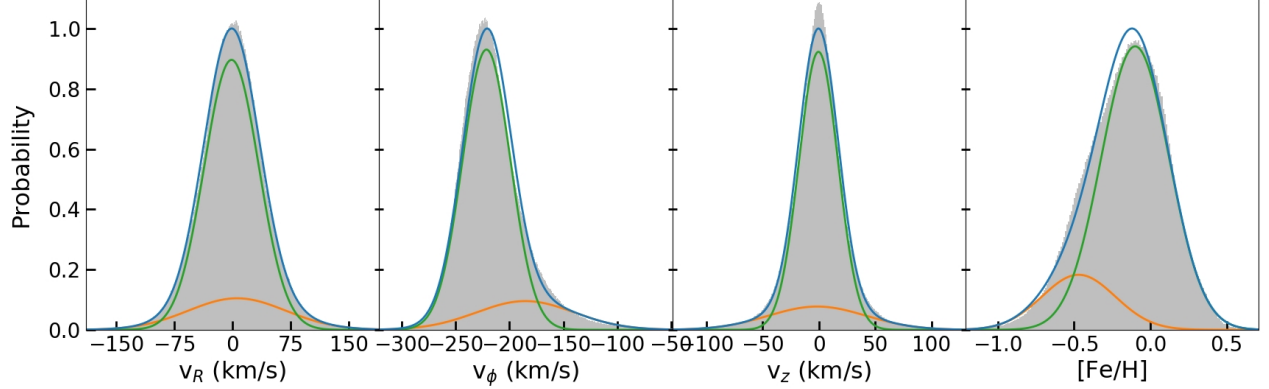


FIG. 1.— Velocity and chemical distribution of disk-classified star cross-matched between Gaia and LAMOST. The observation is shown as gray histogram. The green and orange line represent the thin disk and the thick disk. These components were identified using a two-component Gaussian model. And the blue line shows the total model.

2.3. Decomposition into disk and halo

Selecting halo stars based on metallicity is a common method. Disk stars are metal-rich, with a peak in the metallicity distribution at approximately solar metallicity, $[Fe/H] = 0$. The halo is more metal poor; the inner halo has a typical metallicity of $[Fe/H] = -1.45$ (e.g., Zuo et al. 2017) or $[Fe/H] = -1.6$ (e.g., Allende Prieto et al. 2006). However, Bonaca et al. (2017) use the first Gaia data, combined with the RAVE and APOGEE spectroscopic surveys, to reveal a metal-rich halo component within $\lesssim 3$ kpc from the Sun. They select halo stars kinematically with a relative velocity of at least 220 km s^{-1} with respect to the local standard of rest and find half of their halo sample is comprised of stars with $[Fe/H] > -1$. The metallicity appears to extend even to super-solar values. So we will lose many metal-rich halo stars if we select halo stars by metallicity.

Another commonly used selection criterion for halo stars is $|V - V_{LSR}| > V_{cut}$ in Toomre diagram of Cartesian coordinates. However, the velocity dispersion are different and covariance coefficient are not zero in Cartesian coordinates. If adopting the spherical or cylindrical coordinate system, the diagonal covariance matrix can be applied.

In this work, we use the method provided by Bensby et al. (2003) to obtain the probabilities that a given star belongs to a specific population by assuming the Galactic space velocities and metallicity of the stellar populations in the thin disk, the thick disk, and the halo have Gaussian distributions. Halo stars are too few to be identified obviously as a Gaussian component. So we remove stars with $v_\phi > -40 \text{ km s}^{-1}$ and $[Fe/H] < -1.4$. Then we use the sci-KIT LEARN package in PYTHON (Pedregosa et al. 2012) to fit a two-component Gaussian Mixture Model to the spherical velocities and metallicity of the stars, v_R , v_θ , v_ϕ and $[Fe/H]$. In this fitting, each component has its own diagonal covariance matrix. The velocity dispersion are $(\sigma_R, \sigma_\theta, \sigma_\phi) = (35, 22, 17) \text{ km s}^{-1}$ for the thin disk and $(\sigma_R, \sigma_\theta, \sigma_\phi) = (63, 45, 43) \text{ km s}^{-1}$ for the thick disk. The mean of v_R and v_z are close to 0 km s^{-1} for both thin and thick disk. The mean of v_ϕ is -221 km s^{-1} for the thin disk and -185 km s^{-1} for the thick disk. The mean and dispersion of metallicity are -0.10 , 0.22 for the thin disk and -0.47 , 0.24 for the thick disk. The fitting result is shown in Figure 1 and we get the probability that star belongs to thin disk (D) or thick disk (TD).

Bond et al. (2010) used SDSS data to analyze velocities of

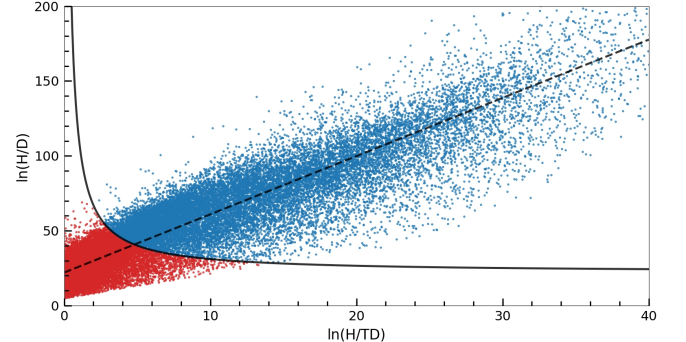


FIG. 2.— Distribution of $\ln(H/D)$ vs $\ln(H/TD)$ for the stars with $H>D$ and $H>TD$. The black dash line is the linear function for fitting $\ln(H/TD)$ and $\ln(H/D)$ using least square method. The halo stars (blue dots) are defined as having $\ln(H/TD) * (\ln(H/D) - b) > 90$, where $b = 22.10$ is the y-intercept and the dividing line is shown in solid black.

about 100 thousand halo stars. They found the mean rotation of halo stars is $\mu_\phi = -(V_{LSR} + V_\odot - 205) \text{ km s}^{-1} = -38.8 \text{ km s}^{-1}$, where $V_{LSR} = 232.8 \text{ km s}^{-1}$ and $V_\odot = 11 \text{ km s}^{-1}$. And the velocity ellipsoid $(\sigma_r, \sigma_\theta, \sigma_\phi) = (141, 75, 85) \text{ km s}^{-1}$ whose principal axes align well with spherical coordinates. Based on the SDSS and SCUSS, (Zuo et al. 2017) found the mean metallicity of inner halo is $\mu_{[Fe/H]} = -1.43$ and the dispersion is $\sigma_{[Fe/H]} = 0.36$. So we can use the four-dimensional Gaussian distribution, i.e.

$$f(v_r, v_\theta, v_\phi, [Fe/H]) = k \cdot \exp \left(-\frac{v_r^2}{2\sigma_r^2} - \frac{v_\theta^2}{2\sigma_\theta^2} - \frac{(v_\phi - \mu_\phi)^2}{2\sigma_\phi^2} - \frac{([Fe/H] - \mu_{[Fe/H]})^2}{2\sigma_{[Fe/H]}^2} \right) \quad (6)$$

where $k = \frac{1}{(2\pi)^2 \sigma_r \sigma_\theta \sigma_\phi \sigma_{[Fe/H]}}$, to get the probability that star belongs to halo (which we call H). Now we can derive two relative probabilities for the halo-to-thin-disk (H/D) and halo-to-thick-disk (H/TD) for each star in our sample. Because of the similarities between the thin disk and the thick disk, when one of $\ln(H/TD)$ and $\ln(H/D)$ is large, the other is generally large. So after selecting stars with $H>D$ and $H>TD$, the least square method is applied to fit line and get the linear relation between $\ln(H/TD)$ and $\ln(H/D)$:

$$\ln(H/D) = 3.89 * \ln(H/TD) + 22.10 \quad (7)$$

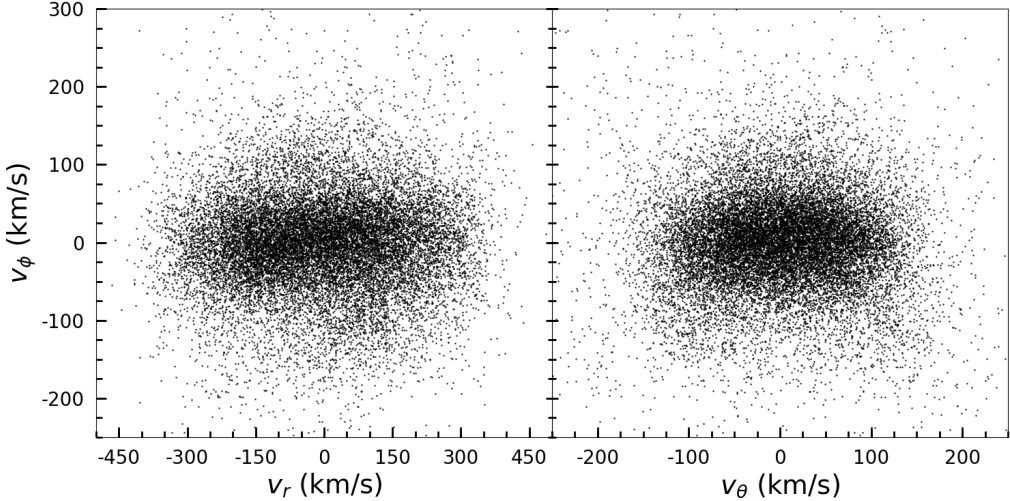


FIG. 3.— Velocities distribution of our halo sample. These stars are classified as belonging to the halo according to a four-component Gaussian model.

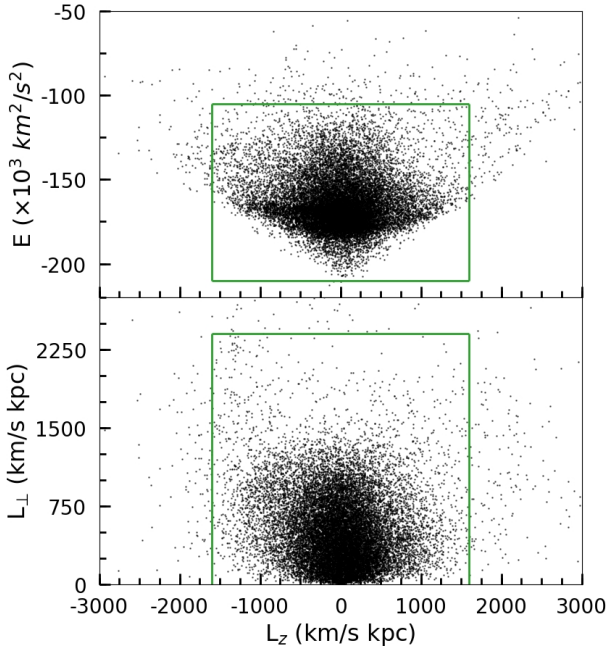


FIG. 4.— Distribution of Energy vs L_z (top panel), and L_{\perp} vs L_z (bottom panel) for the halo sample that was selected in velocity and metallicity from the stars that were in common to both Gaia and LAMOST. The green rectangle shows range of Figure 5.

Then we select sample halo stars with $\ln(H/TD) * (\ln(H/D) - 22.10) > 90$. The result is shown in Figure 2. Our final sample contains 20,089 halo stars, and Figure 3 shows their velocity distribution in spherical coordinates system.

3. SUBSTRUCTURES DETECTION

We now search for local stellar halo substructures in this sample of stars. Models predict that if the halo was built via accretion, the stellar halo in the Solar neighborhood should contain 300-500 streams originating mostly from a handful of massive progenitors (Helmi & White 1999a). The number of streams found in the stellar halo will aid in understanding the role of the past accretion events in the formation of the Milky Way.

We distinguish between two uses of the word “stream” in the literature. One type is dynamical streams, often called “moving groups,” which are groups of stars trapped in a small region of phase space by dynamical resonances. The types stars in such streams, which are often associated with disk resonances, do not depend on their origin, age or type (Dehnen & Binney 1998; Famaey et al. 2005). Dynamical streams tend to be clustered in (U, V) space (Antoja et al. 2008; Zhao et al. 2009, 2014). Klement et al. (2008) and Zhao et al. (2014) detected strams in V and $\sqrt{U^2 + 2V^2}$ space. The other type of stream is tidal streams, which originate from the tidal disruption of accreted satellite galaxies or star clusters. Although the stars in a tidal stream are usually confined to a fraction of the volume of the stellar halo, in a small volume these tidal streams will manifest themselves as a group of stars moving with similar velocities, and in this case tidal streams could be identified as “moving groups” of stars. Helmi et al. (1999b, 2017) used a method of searching for streams in “Integrals of Motion” space, defined by a star’s energy, E , and two components of the angular momentum. Although this technique can in principle be used to link stars in different volumes to the same infall event, it is often used to detect halo streams in the local solar neighborhood (Kepley et al. 2007; Helmi & de Zeeuw 2000; Helmi et al. 2017), because that is the only region for which we presently have 6D phase space information. In this paper, we follow a similar approach to identify local substructure that could correspond to accreted satellites.

3.1. Distribution of stars in Integrals-of-Motion space

For each of the stars in our halo sample, we compute the energy and angular momentum by adopting a Galaxy potential model which is provided by McMillan (2017). Their model includes four components: the cold gas discs near the Galactic plane, the thin and thick stellar discs, a bulge and a dark-matter halo. Figure 4 shows the distribution in energy versus z -angular momentum, L_z , in the upper panel, and the $L_{\perp} = \sqrt{L_x^2 + L_y^2}$ versus L_z on the lower panel for our sample stars. Note that the L_z of retrograde stars is positive. Helmi et al. (2017) found slightly retrograde at $L_z \sim -500 \text{ km s}^{-1} \text{ kpc}$ and a very retrograde orbits with $L_z < -1000 \text{ km s}^{-1} \text{ kpc}$ and they concluded that the retrograde rotation was not an artifact of the errors or even an incorrect value for the circular

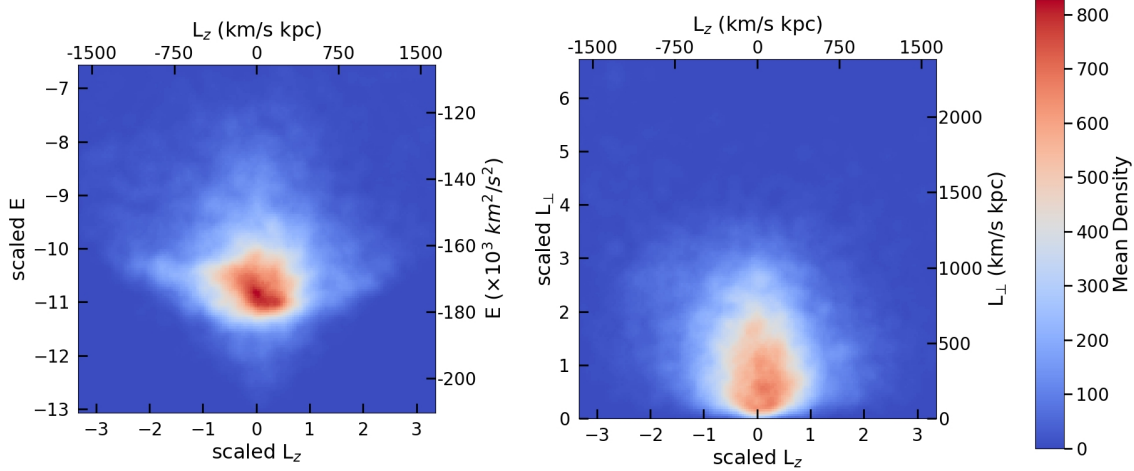


FIG. 5.— Projection of three-dimension kernel density distribution of the halo sample stars in E vs L_z space (left panel), and in L_\perp vs L_z space (right panel). The color corresponds to their mean density on the third axis (L_\perp for the left panel and E for the right panel).

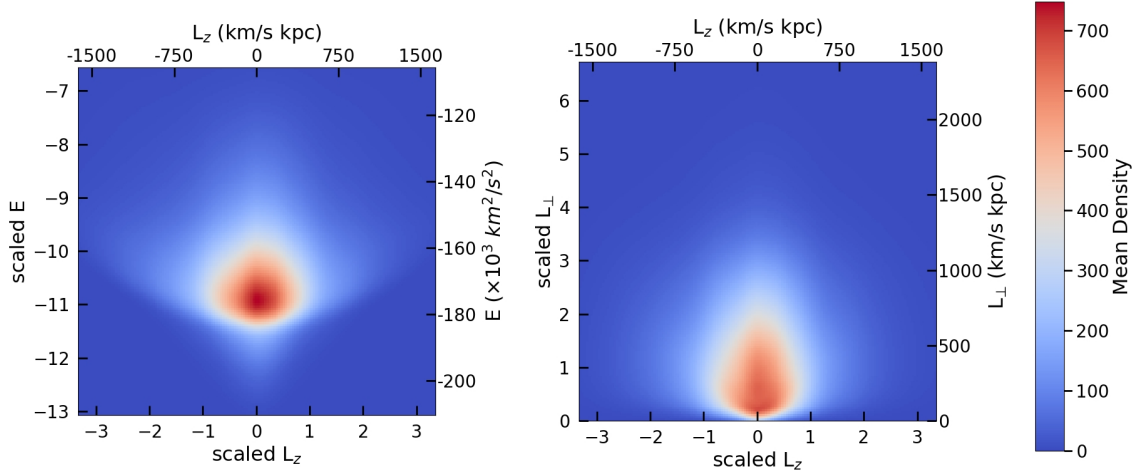


FIG. 6.— As in Figure 5, but now we use average density of all 5000 randomized realizations of the data as the real data.

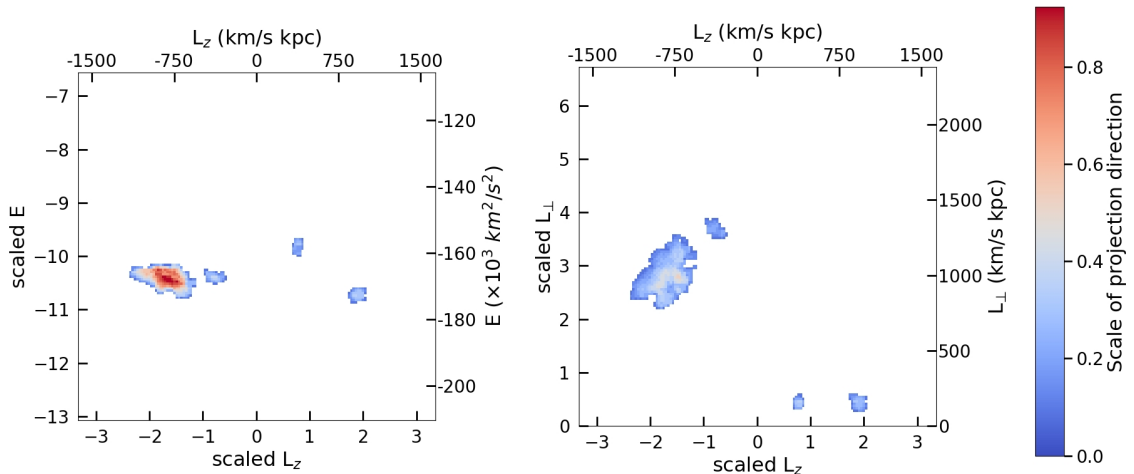


FIG. 7.— To find the candidate of overdensities, we use the Cumulative Distribution Function of Poisson distribution to estimate the significant of pixels. Only the pixels having a significant $> 3.5\sigma$ and $\lambda > 2$ are marked. The color corresponds to their scale length of the third axis.

velocity of the Local Standard of Rest. But in this work, the retrograde rotation is not clear.

3.2. Substructures in the phase-space

In order to constrain our sample in populated region of Figure 4, we select those stars within $-1600 < L_z < 1600 \text{ km s}^{-1} \text{ kpc}$, $-2.10 \times 10^5 < E < -1.05 \times 10^5 \text{ km}^2 \text{ s}^{-2}$, and $L_{\perp} < 2400 \text{ km s}^{-1} \text{ kpc}$. This region is also shown in Figure 4. We apply the sci-KIT LEARN implementation of a non-parametric density estimator that uses an “Tophat” kernel to determine the density field of the stars in $E - L_z - L_{\perp}$ space. We have scaled the data to unit standard deviation to obtain optimal results from the kernel density estimator. The cross-validation method (e.g. Weiss & Kulikowski 1991), also implemented in sci-KIT LEARN, is used to search the optimal bandwidth for the kernel density estimator, and found it to be 0.196. Then we estimate the density which we call kde_{real} . The result is shown in Figure 5. The left panel represents projection of three-dimension kernel density distribution of the halo sample stars in E versus L_z space, and the right is in L_{\perp} versus L_z space. The color corresponds to their mean density on the third axis.

To determine the probability that any overdensities in the real data could happen by chance, we reshuffle the velocity components to create 5,000 randomized datasets. Then we recompute their distribution in $E - L_z - L_{\perp}$ space and use the kernel density estimator with same parameters to get the density. The average density of these randomized datasets is shown in Figure 6. We assume that the part of overdensity is still overdensity, so we use pixels as probes to find the region that might be the overdensity. For each pixel in $E - L_z - L_{\perp}$ space, we can derive the number of stars in a spherical region with a radius of bandwidth from the density of this pixel. We call that number N_{real} for the real data and N_{rand} for the randomized datasets. Using 5000 randomized datasets, we can get the mean of N_{rand} and we call it λ . We use the Cumulative Distribution Function of Poisson distribution,

$$P(X < N) = \sum_{k=0}^{N-1} \frac{\lambda^k}{k!} e^{-\lambda} \quad (8)$$

to estimate the significant of each pixel in real data. Then we select pixels with significant $> 3.5\sigma$ and $\lambda > 2$. We use sci-KIT IMAGE (van der Walt et al. 2014) implementation to remove small bright spots (i.e. the pixel we selected) and connect small dark cracks. We also remove the size of overdensities smaller than 130 pixels. Result of this procedure is shown in Figure 7. Adjacent pixels are considered to belong to the same overdensity. When we perform a similar analysis using 100 random datasets as the real data, we find that only one of them appear one overdensity.

Finally, we identify 4 candidates of overdensities in “Integrals of Motion” space and we extract member stars from the spherical region corresponding to the pixel. We also use the Cumulative Distribution Function of Poisson distribution to estimate the significant of these overdensities. All of the overdensities are identified substructures in this study, and we label them GL-1 through 4. Distribution of member stars in $E - L_z - L_{\perp}$ space are shown in Figure 8. In the Appendix we have tabulated the information of these member stars which belong to substructures. GL-1 has 385 stars, so it not included in the appendix.

Figure 8 also shows the velocity distribution of the member stars in the 4 substructures. Some structures are clustered in

$v_{\phi} - v_{\theta}$ space, but separated in $v_{\phi} - v_r$ space, e.g. GL-3. Or conversely, they are separated in $v_{\phi} - v_{\theta}$ space, but clustered in $v_{\phi} - v_r$ space, e.g. GL-1. This separation may be related to multiple accumulation history. Figure 9 shows the metallicity distribution for these member stars. As shown in left panel of Figure 8, GL-1 and GL-2 are very close in $E - L_z - L_{\perp}$ space, but at their junction, the number of stars is small and the significant of this region is not high enough. In Figure 9, we also can see the difference of these two substructures in [Fe/H], so we consider they are different structures.

3.3. New and old substructures

We compared our substructures with other reported substructures (e.g. Klement et al. 2009; Re Fiorentin et al. 2015) and found a overlap. The substructure GL-1 identified in our sample and “N2” stream (Zhao et al. 2015) have similar [Fe/H], V_{az} and $V_{\Delta E}$. The distributions of the part of GL-1 in our sample are also similar to VelHel-7 of Helmi et al. (2017). It indicate that the streams are probably related to each other, and could originate from the same population. It is not surprising that only one group are found in common with these surveys that using RAVE data, since there is little overlap between the RAVE and the LAMOST dataset. Li et al. (2017) presented the candidate members of the Pal 5, GD-1, Cetus Polar and Orphan tidal stellar streams found in LAMOST DR3, SDSS DR9 and APOGEE catalogs. But we found no overlap between their stellar streams and our substructures. Liang et al. (2017) applied the wavelet transform method to identify 16 significant overdensities in velocity space. Due to the selection effects of sample stars, e.g. different halo samples or the space used to identify the substructure, those star streams found in their surveys are not included completely in our cross-matched data set. In summary, the significant, mean energy, L_z and L_{\perp} of 4 structures are shown in the Table 1. A catalog of 3 substructures’ members (except the largest structure) are given in the Appendix.

TABLE 1 The center of the overdensities in our sample

Notation	significant	E ($\times 10^3 \text{ km}^2 \text{ s}^{-2}$)	L_z ($\text{km s}^{-1} \text{ kpc}$)	L_{\perp} ($\text{km s}^{-1} \text{ kpc}$)
GL-1	$> 10\sigma$	-167.6	-808.8	977.8
GL-2	5.17σ	-166.9	-367.8	1284.0
GL-3	4.18σ	-158.3	370.8	156.4
GL-4	5.10σ	-172.8	903.9	165.8

4. CONCLUSIONS

By cross-matching the Gaia DR2 and LAMOST DR5 data, we obtain a sample of stars with full phase-space information and identified a subset sample halo stars kinematically and chemically. Our final halo sample consists of 20,089 stars. We determine the distribution of the sample halo stars in “Integrals-of-Motion” space, defined by two components of the angular momentum, L_{\perp} and L_z , and by energy. We find some overdensities in this space. To remove the contamination, we estimate the statistical significance for these overdensities and identify 4 substructures. Three of the 4 significant structures are not reported in previous works. One structure may correspond to the “N2” stream of Zhao et al. (2015) and VelHel-7 of Helmi et al. (2017). The identified structures may be the debris from satellite accretion events, their dynamical and chemical properties can aid in understanding the history of the Milky Way.

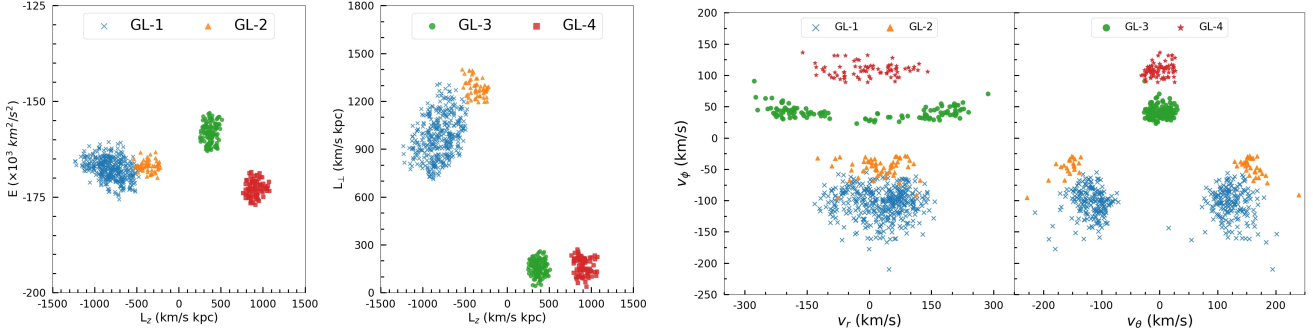


FIG. 8.— Distribution in $E - L_z - L_{\perp}$ (left panel) and spherical velocities (right panel) space, for the stars comprising the identified substructures.

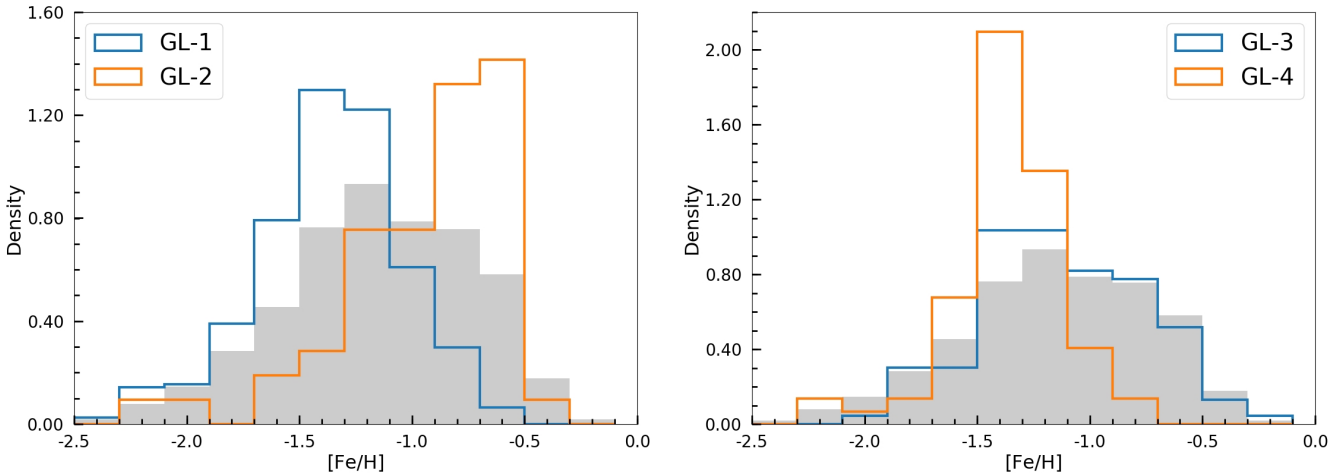


FIG. 9.— Metallicity distribution for the member stars of comprising the identified substructures. Halo sample is shown as gray histogram.

5. ACKNOWLEDGEMENTS

We thank especially the referee for insightful comments and suggestions, which have improved the paper significantly. This work has made use of data from the European Space Agency (ESA) mission *Gaia* (<https://www.cosmos.esa.int/gaia>), processed by the *Gaia* Data Processing and Analysis Consortium (DPAC, <https://www.cosmos.esa.int/web/gaia/dpac/consortium>). Funding for the DPAC has been provided by national institutions, in particular the institutions participating in the *Gaia* Multilateral Agreement.

This work was supported by joint funding for Astronomy by the National Natural Science Foundation of China and the Chinese Academy of Science, under Grants U1231113. This

work was also by supported by the Special funds of cooperation between the Institute and the University of the Chinese Academy of Sciences, and China Scholarship Council (CSC). HJN acknowledges funding from NSF grant AST-1615688. Funding for SDSS-III has been provided by the Alfred P. Sloan Foundation, the Participating Institutions, the National Science Foundation, and the U.S. Department of Energy Office of Science. This project was developed in part at the 2016 NYC Gaia Sprint, hosted by the Center for Computational Astrophysics at the Simons Foundation in New York City. The Guoshoujing Telescope (LAMOST) is a National Major Scientific Project has been provided by the National Development and Reform Commission. LAMOST is operated and managed by the National Astronomical Observatories, Chinese Academy of Sciences.

REFERENCES

- Abadi, M. G., Navarro, J. F., & Steinmetz, M. 2003, ApJ, 597, 21
- Allende Prieto, C., Beers, T. C., Wilhelm, R., et al. 2006, ApJ, 636, 804
- Antoja, T., Figueras, F., Fernandez, D., et al. 2008, A&A, 490, 135
- Antoja, T., Helmi, A., Bienayme, O., et al. 2012, MNRAS, 426, L1
- Bailer-Jones, C. A. L., Rybizki, J., Fouesneau, M., et al. 2018, AJ, 156, 58
- Belokurov, V., Erkal, D., Evans, N. W., et al. 2018, MNRAS, 478, 611
- Belokurov, V., Evans, N. W., Irwin, M. J., et al. 2007, ApJ, 658, 337
- Belokurov, V., Zucker, D. B., Evans, N. W., et al. 2006, ApJ Lett, 642, L137
- Bensby, T., Feltzing, S., & Lundstrm, I. 2003, A&A, 410, 527
- Bland-Hawthorn, J., & Gerhard, O. 2016, ARA&A, 54, 529
- Bonaca, A., Conroy, C., Wetzel, A., et al. 2017, ApJ, 845, 101
- Bond, N. A., Ivezić, Ž., Sesar, B., et al. 2010, ApJ, 716, 1
- Bullock, J. S., & Johnston, K. V. 2005, ApJ, 635, 931
- Carollo, D., Beers, T. C., Lee, Y. S., et al. 2007, Nature, 450, 1020
- Carollo, D., Beers, T. C., Chiba, M., et al. 2010, ApJ, 712, 692
- Chiba, M., & Beers, T. C. 2000, AJ, 119, 2843
- Cooper, A. P., Parry, O. H., Lowing, B., et al. 2015, MNRAS, 454, 3185
- Cui, X. Q., Zhao, Y. H., Chu, Y. Q., et al. 2012, RAA, 12, 1197
- Deason, A. J., Belokurov, V., Koposov S. E., et al. 2017, MNRAS, 470, 1259
- Dehnen, W., & Binney, J. J. 1998, MNRAS, 298, 387
- Deng, L. C., Newberg, H. J., Liu C., et al. 2012, RAA, 12, 735
- Diemand, J., Kuhlen, M., Madau, P., et al. 2008, Nature, 454, 735
- Duffau, S., Vivas, A. K., Zinn, R., et al. 2014, A&A, 566, A118
- Duffau, S., Zinn, R., Vivas, A. K., et al. 2006, ApJ Lett, 636, L97
- Eggen, O. J., Lynden-Bell, D., & Sandage, A. R. 1962, ApJ, 136, 748

- Famaey, B., Jorissen, A., Luri, X., et al. 2005, *A&A*, 430, 165
- Fernández-Trincado, J. G., Robin, A. C., Vieira, K., et al. 2015, *A&A*, 583, A76
- Font, A. S., McCarthy, I. G., Crain, R. A., et al. 2011, *MNRAS*, 416, 2802
- Freeman, K., & Bland-Hawthorn, J. 2002, *ARA&A*, 40, 487
- Gaia Collaboration, (Brown, A. G. A., et al.) 2018, *A&A*, 616, A1
- Grillmair, C. J., & Carlin, J. L. 2016, *ASSL*, 420, 87
- Grillmair, C. J. 2006, *ApJ Lett*, 645, L37
- Helmi, A., Veljanoski J., Breddels M. A., et al. 2017, *A&A*, 598, A58
- Helmi, A., & de Zeeuw, P. T. 2000, *MNRAS*, 319, 657
- Helmi, A., & White, S. D. M. 1999a, *MNRAS*, 307, 495
- Helmi, A., White S. D. M., de Zeeuw P. T., et al. 1999b, *Nature*, 402, 53
- Huang, Y., Liu, X. W., Chen, B. Q., et al. 2018, *AJ*, 156, 90
- Ibata, R. A., Gilmore, G., Irwin, M. J. 1994, *Nature*, 370, 194
- Johnson, D. R. H., & Soderblom, D. R. 1987, *AJ*, 93, 864
- Jurić M., Ivezić, Ž., Brooks, A., et al. 2008, *ApJ*, 673, 864
- Kepley, A. A., Morrison, H. L., Helmi, A., et al. 2007, *AJ*, 134, 1579
- Klement, R., Fuchs, B., & Rix, H. W. 2008, *ApJ*, 685, 261
- Klement, R. J. 2010, *A&A Rev.*, 18, 567
- Klement, R., Rix, H. W., Flynn, C., et al. 2009, *ApJ*, 698, 865
- Klypin, A. A., Trujillo-Gomez, S., & Primack, J. 2011, *ApJ*, 740, 102
- Kordopatis, G., Gilmore, G., Wyse, R. F. G., et al. 2013, *MNRAS*, 436, 3231
- Li, G. W., Yanny, B., Zhang, H. T., et al. 2017, *RAA*, 17, 62
- Liang, X. L., Zhao, J. K., Oswalt, T. D., et al. 2017, *ApJ*, 844, 152
- Lindgren, L., Hernández, J., Bombrun, A., et al. 2018, *AJ*, 616, A2
- Lindgren, L., Lammers, U., Bastian, U., et al. 2016, *A&A*, 595, A4
- Luri, X., Brown, A. G. A., Sarro, L. M., et al. 2018, *A&A*, 616, A9
- Luo, A. L., Zhao, Y. H., Zhao, G., et al. 2015, *RAA*, 15, 1095
- Majewski, S. R., Skrutskie, M. F., Weinberg, M. D., et al. 2003, *ApJ*, 599, 1082
- McMillan, P. J., 2017, *MNRAS*, 465, 76
- Morrison, H. L., Helmi, A., Sun, J.-Y., et al. 2009, *ApJ*, 694, 130
- Newberg, H. J., Willett, B. A., Yanny, B., & Xu, Y. 2010, *ApJ*, 711, 32
- Newberg, H. J., Yanny, B., Cole, N., et al. 2007, *ApJ*, 668, 221
- Pedregosa, F., Varoquaux, G., Gramfort, A., et al. 2012, arXiv:1201.0490
- Re Fiorentin, P., Lattanzi, M. G., Spagna, A., et al. 2015, *AJ*, 150, 128
- Sales, L. V., Navarro, J. F., Abadi, M. G., et al. 2007, *MNRAS*, 379, 1464
- Searle, L., & Zinn, R. 1978, *ApJ*, 225, 357
- Skrutskie, M. F., Schneider, S. E., Stiening, R., et al. 1997, *ASSL*, 210, 25
- Smith, M. C., Evans, N. W., Belokurov, V., et al. 2009, *MNRAS*, 399, 1223
- Springel, V., Wang, J., Vogelsberger, M., et al. 2008, *MNRAS*, 391, 1685
- Steinmetz, M., Zwitter, T., Siebert, A., et al. 2006, *AJ*, 132, 1645
- Tissera, P. B., Beers, T. C., Carollo, D., et al. 2014, *MNRAS*, 439, 3128
- Tian, H. J., Liu, C., Carlin, J. L., et al. 2015, *ApJ*, 809, 145
- van der Walt, S., Schönberger, J. L., Nunez-Iglesias, J., et al. 2014, *PeerJ*, 2, 453
- van Leeuwen, F. 2007, *ASSL*, 350
- Vincent, L., & Soille, P. 1991, *KvanE*, 13, 583
- Weiss, S., & Kulikowski, C. 1991, Computer Systems that Learn: Classification and Prediction Methods from Statistics, Neural Nets, Machine Learning, and Expert Systems
- Wright, E. L., Eisenhardt, P. R. M., Mainzer, A. K., et al. 2010, *AJ*, 140, 1868
- Wu, Y., Luo, A. L., Li, H. N., et al. 2011, *RAA*, 11, 924
- York, D. G., Adelman, J., Anderson, J. E., Jr., et al. 2000, *AJ*, 120, 1579
- Zhao, G., Zhao, Y.-H., Chu, Y.-Q., et al. 2012, *RAA*, 12, 723
- Zhao, J. K., Zhao, G., & Chen, Y. Q. 2009, *ApJ Lett*, 692, L113
- Zhao, J. K., Zhao, G., Chen, Y. Q., et al. 2014, *ApJ*, 787, 31
- Zhao, J. K., Zhao, G., Chen, Y. Q., et al. 2015, *RAA*, 15, 1378
- Zolotov, A., Willman, B., Brooks, A., et al. 2010, *ApJ*, 721, 738
- Zuo, W.B., Du, C.H., Jing, Y.J., et al. 2017, *ApJ*, 841, 59

APPENDIX

MEMBER STARS OF THE NEW IDENTIFIED SUBSTRUCTURES

Unique source identifiers in Gaia and LAMOST, positions, metallicities, space velocities and z-angular momentum for the member stars.

TABLE 2 GL-2, 53 stars

source-id	obsid	<i>l</i> (deg)	<i>b</i> (deg)	[Fe/H] (dex)	<i>x</i> (kpc)	<i>y</i> (kpc)	<i>z</i> (kpc)	<i>U</i> (km s ⁻¹)	<i>V</i> (km s ⁻¹)	<i>W</i> (km s ⁻¹)	<i>L_z</i> (km s ⁻¹ kpc)
3662032469693724800	572211196	331.38	59.02	-1.31	6.0	1.2	4.2	10.8	48.8	193.2	-278.3
2503115396900046720	209808189	166.72	-51.47	-0.64	8.6	-0.1	-0.5	-64.2	31.5	-154.8	-264.6
1231233915353158528	120207106	1.90	69.06	-0.83	7.9	-0.0	0.9	-61.4	57.0	-169.9	-447.1
1285189081231978752	233011085	49.30	69.95	-1.20	7.9	-0.4	1.3	-18.9	47.7	-166.3	-369.4
1286611711842881024	227006099	53.82	64.70	-0.51	7.8	-0.6	1.5	52.9	28.9	-171.9	-254.6
1484880665082822528	422712018	71.79	68.72	-1.63	8.1	-0.3	0.9	-44.7	45.5	170.8	-354.3
1545642735656223744	448503191	138.17	67.81	-0.89	8.5	-0.3	1.1	-17.4	38.4	-146.4	-322.9
3886582740137269248	275101172	225.58	58.38	-0.55	8.9	0.7	1.6	-94.6	30.8	-125.5	-338.4
1247776480110134272	450215050	0.84	75.26	-0.94	7.7	-0.0	2.1	-51.5	68.2	-153.2	-522.1
2653377439090572928	362206040	70.94	-50.33	-1.13	7.7	-1.4	-1.8	-120.9	58.1	130.4	-278.9
4368228034935117184	457401037	19.41	21.30	-1.17	4.6	-1.3	1.5	-150.1	135.7	-194.0	-432.3
4386425158532864384	327606021	22.57	28.14	-1.44	4.6	-1.5	2.1	182.3	40.7	179.2	-460.1
4408486687546910464	552612050	13.43	33.77	-0.43	6.8	-0.3	1.0	-89.3	71.8	207.5	-455.8
4446871703622166144	240813081	27.43	33.82	-1.25	6.7	-0.8	1.1	-70.9	49.4	193.7	-277.8
445160434526684160	233105084	19.65	40.92	-0.67	7.4	-0.3	0.7	109.0	28.0	-172.0	-238.2
2120723115527908096	155706110	77.60	22.84	-2.24	7.4	-3.6	1.6	-19.3	42.1	161.4	-241.4
291660753646824320	267302070	136.30	-37.55	-0.64	8.6	-0.4	-0.4	-65.1	57.8	135.3	-472.1
2747259239428992000	182916121	110.41	-56.70	-0.83	8.4	-0.6	-0.9	108.3	37.1	-137.5	-375.2
2801278108262214912	245308088	121.43	-42.88	-0.56	8.7	-0.8	-0.8	-26.4	43.1	146.5	-353.8
2835956705002706176	353313048	89.90	-33.05	-0.55	8.2	-1.1	-0.7	-68.1	38.0	-161.8	-234.3
2864046890629860480	81903062	115.83	-28.38	-0.59	8.7	-1.0	-0.6	-18.1	52.4	145.6	-436.7
3390618402335173632	374410052	188.43	-12.29	-0.58	8.8	0.1	-0.1	69.1	31.2	136.8	-269.2
3719566167963752576	346103184	332.39	68.58	-1.30	8.0	0.1	0.5	15.7	63.2	-172.0	-505.8
3729537260959070848	422111089	314.63	69.49	-1.27	7.9	0.3	1.2	-45.0	48.9	-168.2	-399.7
382302247690095104	415910187	242.85	37.42	-0.91	8.6	0.8	0.7	5.6	34.4	155.0	-292.1
3858667372562954880	215105115	242.23	51.56	-0.85	8.5	0.6	0.9	-15.4	39.0	141.2	-340.7
3879706050819568384	484603106	224.86	45.27	-0.82	8.8	0.6	0.8	-3.5	43.4	148.0	-382.6
98563009748281472	378512245	141.66	-37.88	-0.65	8.7	-0.4	-0.5	-23.0	49.1	-158.1	-419.2
586365363499961728	223808024	225.52	37.43	-0.71	8.4	0.2	0.3	-68.5	27.9	-148.8	-250.7
598769607008444672	420802068	216.12	29.88	-0.52	8.9	0.5	0.6	30.2	43.7	-144.3	-374.6
659641078984352384	400306238	207.10	31.27	-0.93	8.5	0.2	0.2	-23.0	56.4	155.5	-483.0
726491312936718208	139813093	208.51	53.61	-1.17	8.6	0.2	0.7	-2.0	33.1	147.1	-286.3
760791200935729792	450115068	177.30	69.55	-1.70	8.4	-0.0	0.5	33.9	51.3	-151.5	-431.0
124672074278894320	558005076	9.84	73.36	-0.57	7.5	-0.1	2.3	-114.3	33.9	-127.9	-242.8
1278545935057357824	350215109	53.58	57.10	-1.26	7.1	-1.5	3.0	-94.1	75.8	-133.9	-392.6
1336301837755473280	462608072	60.77	31.54	-2.06	6.5	-3.0	2.1	111.8	23.5	143.8	-486.0
1491909293163433344	575415144	76.31	67.28	-0.95	8.1	-0.3	0.8	-43.1	55.0	-160.3	-433.4
1525146464518953088	210910197	98.93	74.21	-1.21	8.2	-0.1	0.5	-65.4	39.8	-145.8	-318.3
1590711339315440512	418016063	83.85	59.06	-0.51	8.1	-0.7	1.1	-31.1	47.9	153.7	-368.8
1731977452245467520	370212003	53.87	-28.37	-0.70	6.5	-2.3	-1.5	-5.8	78.1	-196.2	-496.4
1739454062594964352	469604140	60.53	-29.61	-0.81	7.9	-0.5	-0.3	-54.4	51.5	157.4	-378.4
1864801343109259904	475212086	75.34	-9.32	-0.84	7.3	-3.5	-0.6	16.2	49.0	-172.9	-413.6
1304558662184239232	225006050	47.15	39.74	-0.74	7.7	-0.6	0.7	-103.6	36.9	-158.7	-220.9
2511535418290211328	384306035	154.75	-56.42	-1.01	8.4	-0.1	-0.4	9.3	52.6	158.2	-444.8
912354579562114816	181801156	181.48	37.88	-0.78	8.6	0.0	0.3	-57.6	42.7	-150.0	-366.8
4009658429618705152	332707210	209.88	82.20	-0.72	8.6	0.2	3.0	-50.5	43.3	-123.8	-380.4
4006785027777824384	332705203	207.35	80.19	-1.03	8.5	0.1	1.7	-27.0	36.7	-147.3	-314.3
1740820648172737280	377801243	63.00	-31.39	-0.76	7.4	-1.6	-1.1	19.0	57.0	-183.5	-451.1
612386543123006336	554316077	209.21	36.83	-0.54	9.4	0.7	1.1	-3.8	37.3	-130.1	-354.5
3693711839232555008	208504143	293.01	60.12	-0.63	7.8	0.8	1.6	-94.4	49.6	-139.3	-468.6
604279569012986752	94015151	217.25	35.20	-0.96	8.4	0.2	0.2	13.1	30.5	149.1	-255.1
2746111727246997376	505912064	99.03	-53.83	-0.96	8.3	-0.9	-1.2	18.4	37.4	-144.9	-328.3
133443366875832832	388104051	148.95	-25.45	-0.72	8.5	-0.2	-0.1	-35.5	63.9	-166.0	-535.4

TABLE 3 GL-3, 116 stars

source-id	obsid	l (deg)	b (deg)	[Fe/H] (dex)	x (kpc)	y (kpc)	z (kpc)	U (km s ⁻¹)	V (km s ⁻¹)	W (km s ⁻¹)	L _z (km s ⁻¹ kpc)
776435773930211328	142613029	178.19	62.15	-0.68	11.0	-0.1	5.2	30.4	-23.3	-7.4	252.6
2521025925920389504	266810185	154.78	-50.88	-1.19	8.9	-0.3	-0.9	187.1	-47.2	-4.0	360.2
3955108049991504512	101501160	288.27	84.94	-1.73	8.2	0.0	0.5	215.9	-42.5	9.4	357.5
599099323058438016	313815016	216.50	24.85	-0.91	10.1	1.4	1.1	152.6	-11.5	-18.8	336.5
605566719171720960	502101137	214.54	33.94	-1.42	8.9	0.5	0.6	193.7	-28.2	-26.5	344.4
711037268988125312	130104169	189.83	35.60	-1.35	10.5	0.4	1.7	139.2	-35.8	-30.4	431.7
786574954766550784	146707169	148.02	66.27	-1.25	9.1	-0.6	2.5	142.2	-47.0	-19.2	346.8
790728561803079168	314703069	149.31	63.35	-1.49	8.6	-0.3	1.0	-209.8	-44.3	-3.7	437.5
828495278684213888	293914160	162.09	48.50	-0.92	10.9	-0.9	3.2	105.3	-48.7	-41.3	438.4
829090492436805504	343413114	173.15	57.62	-1.08	10.6	-0.3	3.8	97.7	-42.7	-17.1	423.8
16689140394921344	279604032	165.36	-17.94	-0.84	10.8	-0.7	-0.8	147.9	-56.5	24.5	509.9
1533388334960428672	132809043	143.96	75.07	-0.80	9.1	-0.6	4.1	105.7	-42.9	-42.1	321.6
1542725937461194752	319209158	126.81	70.32	-0.38	8.8	-0.8	2.9	-163.5	-25.6	62.1	358.4
1545461281877377664	145105114	136.24	68.61	-1.16	8.5	-0.2	0.9	-219.0	-40.1	48.6	391.0
1554494044772634368	149701075	111.65	68.51	-0.88	8.7	-1.3	3.7	-127.2	-30.3	63.7	435.4
1597431554384379264	153713095	85.61	47.67	-0.99	8.1	-1.1	1.3	215.2	-68.1	-53.8	309.4
4471882393403103232	347705157	33.08	12.77	-0.96	4.4	-2.5	1.1	196.9	-215.1	-31.1	459.1
691295881309324800	107208219	198.03	36.56	-1.55	11.5	1.1	2.6	-19.7	-40.9	-11.2	447.7
64932095766434560	337414159	211.93	25.54	-0.82	11.1	1.8	1.7	-124.3	-56.2	30.7	398.3
2825552026469603968	253004025	97.20	-38.41	-1.34	8.6	-2.8	-2.2	133.8	-84.8	43.6	350.3
4391534863945071616	449915052	23.88	26.25	-1.14	3.8	-1.9	2.4	-253.9	51.0	140.8	300.6
4422824525328500224	564606181	7.49	41.40	-0.72	6.3	-0.2	1.7	252.1	-54.9	-93.5	283.2
4427480132438480384	135310139	9.04	44.96	-1.09	7.3	-0.1	0.9	-237.4	-36.8	33.4	302.9
4453040131355904768	236616049	22.02	39.17	-1.30	6.3	-0.8	1.7	229.0	-91.2	-79.8	406.1
4543000115454359808	342805021	38.60	24.33	-1.29	3.8	-3.5	2.5	140.2	-214.3	-116.5	337.9
2130702527879104512	354401051	77.72	17.35	-1.44	7.0	-5.3	1.7	117.9	-145.4	-53.5	394.6
2145762126325789440	153801182	81.48	24.30	-1.73	7.3	-6.0	2.8	77.7	-113.1	-26.2	361.2
2149435629033487744	155308036	81.63	27.82	-1.87	7.5	-4.6	2.5	130.1	-127.9	-36.3	365.4
2150266000831014400	155311112	84.07	28.90	-0.82	8.0	-2.2	1.2	184.2	-97.3	-32.9	372.6
2704791427439158912	247805073	71.19	-45.24	-1.05	7.7	-1.5	-1.6	188.4	-87.1	26.4	377.8
2733432605831478144	174808087	81.93	-36.55	-0.55	7.9	-2.0	-1.5	183.0	-89.5	64.0	334.8
2735977288054696832	480805041	79.68	-35.88	-1.37	8.1	-0.5	-0.4	-210.5	-30.3	8.6	360.1
2805435082553510400	10805107	125.24	-36.66	-0.42	10.7	-3.5	-3.2	84.9	-72.9	31.1	479.8
2807439668344927104	194514093	117.85	-37.82	-1.44	9.9	-3.2	-2.8	74.3	-56.6	41.0	321.4
317684059276916608	362611053	135.59	-27.40	-1.17	10.8	-2.6	-1.9	94.0	-58.8	20.9	394.4
320491597794951936	283908194	130.96	-26.80	-1.41	8.7	-0.6	-0.4	-188.2	-27.8	-18.4	346.8
3064855269056385152	196807059	230.42	18.51	-0.54	11.1	3.5	1.6	15.9	-26.9	-15.1	354.9
3073650979825727616	137205087	226.14	22.84	-1.43	9.5	1.4	0.8	166.0	-17.0	-29.9	387.5
3139910578471472000	492403159	212.18	8.94	-1.17	11.2	1.9	0.6	-137.7	-55.8	22.3	366.4
3360380664340716544	270704186	200.26	12.22	-0.94	9.9	0.6	0.4	181.7	-21.3	13.9	322.8
381409077459596800	176615070	120.08	-21.46	-1.23	8.3	-0.2	-0.1	-219.0	-25.2	23.1	262.2
3632411557722152320	414715155	326.41	54.72	-1.61	7.8	0.3	0.7	214.0	-50.1	-5.7	448.9
37110972763038252032	212911054	323.46	61.49	-1.10	6.7	1.1	3.5	-163.5	-78.4	86.0	337.6
3734233034603510144	342107109	315.26	72.02	-1.20	7.4	0.8	3.5	174.9	-26.4	-64.0	334.2
3884500604416157056	387510031	232.25	56.94	-1.36	8.3	0.2	0.3	-203.2	-58.6	24.2	455.9
3885678597981496192	331909154	228.54	56.64	-1.34	8.8	0.7	1.4	-204.8	-51.3	14.5	314.6
3945085589188023424	405505032	349.01	85.25	-1.05	7.9	0.1	3.4	189.8	-35.0	-98.6	287.7
4018063508817588864	507105216	209.70	74.14	-0.92	8.3	0.1	0.4	223.1	-32.5	-22.9	280.8
4023554332447594624	205031100	195.97	71.72	-0.72	8.3	0.0	0.3	225.3	-38.5	-31.6	325.4
586009671488680320	223705163	225.29	36.69	-1.45	8.5	0.3	0.4	-206.4	-47.7	26.0	338.1
686132643423960448	398004026	204.19	36.86	-1.08	11.4	1.4	2.6	123.8	-23.8	-13.6	448.8
722295477781603200	308501029	213.17	57.78	-0.77	8.6	0.2	0.7	-207.8	-58.3	6.6	449.8
785873466350271360	563009040	153.66	64.26	-0.56	9.0	-0.4	1.9	-170.5	-20.9	15.9	255.7
785710463748905600	140703021	157.44	64.19	-1.20	9.3	-0.4	2.4	-177.4	-31.8	45.8	375.0
826632431109291648	208413191	166.90	49.67	-1.25	10.3	-0.5	2.6	-123.8	-26.5	31.4	333.1
831609885892678016	279407199	161.50	60.22	-1.15	8.3	-0.0	0.1	222.0	-46.1	-34.2	376.1
892040453700593208	314412112	187.64	21.29	-0.63	11.9	0.5	1.5	-42.8	-35.0	15.3	396.2
927844606749721984	318004152	177.49	32.35	-0.62	9.3	-0.0	0.7	188.9	-33.4	-38.5	300.5
1022930028722544128	265809105	163.30	43.89	-0.76	9.8	-0.5	1.6	-150.9	-21.9	42.5	284.8
1024562769129570688	528303141	158.89	42.00	-0.74	9.1	-0.4	0.9	-196.0	-29.4	8.6	340.1
1193391920583495552	347607079	28.35	46.27	-1.05	7.9	-0.2	0.4	-228.7	-42.2	-8.1	370.0
1252847736974969600	136181145	21.77	69.49	-1.15	6.8	-0.6	4.0	183.2	-71.9	-93.2	388.0
1287943254781596160	227015146	58.31	65.94	-0.82	7.4	-1.2	3.3	183.0	-87.8	-81.3	429.3
1327550721630335872	555009234	57.17	41.86	-1.23	7.3	-1.4	1.5	214.9	-106.9	-40.6	477.0
1331866403552107008	48814092	63.18	42.19	-1.26	6.9	-2.6	2.7	193.1	-124.1	-76.9	351.4
1361879708033005952	144807156	72.03	33.63	-1.04	6.9	-4.2	2.9	138.0	-151.7	-78.1	465.6
1415072534396049280	145408225	78.44	34.75	-0.84	7.2	-5.0	3.5	-148.5	44.8	73.3	413.6
1460842866998627840	301804060	62.86	87.59	-1.41	8.2	-0.1	1.6	203.8	-61.5	-44.7	490.3
1483498922564228608	419503232	69.76	71.98	-0.48	7.9	-0.9	3.0	159.8	-64.9	-68.5	368.0
1493366588450862976	128409018	77.42	63.23	-1.40	7.9	-1.4	2.9	-183.8	-10.5	58.9	346.5
1514561500437195776	298106062	143.43	83.88	-1.20	8.3	-0.1	1.3	191.7	-46.1	-42.6	367.2
1522631400389533568	308708228	109.02	79.13	-1.31	8.2	-0.1	0.4	192.3	-57.0	-35.1	454.8
1560427043875297536	397909218	109.92	62.89	-0.90	8.6	-1.1	2.2	-172.2	-34.1	47.8	475.8
1589977346585245056	418004010	80.72	59.12	-1.26	7.8	-2.6	4.4	133.5	-89.9	-100.7	357.3
1600092647401514368	446808094	89.11	52.30	-1.41	8.2	-2.6	3.4	-145.0	-0.0	53.3	376.3
1612828153147112448	564306079	94.30	52.24	-1.00	8.3	-1.1	1.5	214.4	-76.5	-27.0	396.4

39069122766561920	381902155	177.21	-27.52	-1.24	10.5	-0.1	-1.2	112.2	-41.5	5.4	422.1
1760073066712199680	371605087	62.28	-21.05	-0.56	5.8	-4.5	-1.9	-189.5	80.6	-41.2	383.8
1893918575666556416	469702033	87.17	-24.00	-1.70	8.0	-4.5	-2.0	127.1	-128.4	54.6	446.0
217189761654075520	472511147	160.67	-16.11	-1.72	12.8	-1.6	-1.4	-3.7	-27.3	7.3	355.5
1907573200116557312	178415015	93.52	-17.60	-0.74	8.3	-1.8	-0.5	-210.4	3.3	-31.3	348.7
1939324695044566400	182610080	111.15	-13.73	-1.55	10.2	-5.3	-1.4	-97.4	10.7	-12.5	401.9
3155410389590889856	369612136	208.52	10.89	-1.42	8.4	0.1	0.1	208.2	-27.8	17.4	255.6
916214002815131520	496906047	177.57	34.46	-0.69	9.9	-0.1	1.2	-129.5	-43.9	26.5	443.9
3892974510467742080	237709247	274.63	63.71	-0.30	8.2	0.5	1.1	219.4	-22.2	-43.1	295.2
3844841563599413760	296304241	230.31	35.74	-1.30	9.2	1.2	1.2	175.6	-24.9	-38.8	442.9
828272077823821184	442003208	162.29	49.36	-0.77	10.3	-0.7	2.5	-159.4	-34.6	19.7	460.0
2117423618572646528	365016133	73.97	19.67	-1.62	7.6	-2.1	0.8	-233.1	6.5	5.7	446.8
2748328170890349184	181312168	107.44	-55.64	-1.66	8.5	-0.8	-1.3	188.9	-65.1	51.6	393.1
804217031156736000	547602063	180.67	55.70	-1.95	10.8	0.0	3.9	-70.1	-36.2	37.0	389.6
842617680909921408	397809151	152.03	57.83	-1.50	8.8	-0.3	1.1	-204.0	-30.2	11.7	333.5
3098112983239720064	308415134	215.18	23.01	-1.23	9.0	0.6	0.5	-173.3	-48.6	-6.0	336.2
6852850917577994624	187405157	205.90	39.41	-1.88	10.2	1.0	1.8	-118.1	-44.1	4.8	335.2
974643017084542336	182201020	171.87	25.01	-1.12	11.7	-0.5	1.7	-6.1	-28.9	-11.8	342.4
721601548505308928	448215132	214.04	59.20	-1.65	9.2	0.7	2.1	177.5	-21.0	-51.5	317.5
1571249502467492992	152801087	125.40	61.99	-1.44	9.5	-1.8	4.2	-129.4	-6.2	71.3	292.4
1492666547437694464	569710210	79.10	65.84	-1.14	8.0	-1.1	2.6	-218.2	-14.1	48.8	358.5
1293408205528224512	457905178	58.69	63.05	-1.08	7.3	-1.4	3.3	-198.7	-1.1	77.2	288.4
740747516278184576	339902204	199.71	54.45	-0.94	9.5	0.5	2.0	148.0	-33.6	-24.9	388.2
39345031464898304	254103211	176.36	-27.63	-0.83	10.7	-0.2	-1.3	153.5	-38.0	38.9	381.9
884525394804288384	524204063	188.64	15.61	-1.86	11.7	0.5	1.0	-11.3	-29.3	13.8	336.5
140259720489824768	496804234	149.43	-21.54	-1.40	10.6	-1.4	-1.1	-138.2	-12.7	1.5	329.3
3916715165534162048	339504190	253.13	68.65	-0.61	8.3	0.5	1.3	-210.7	-65.2	13.3	440.9
836462443019621120	397803185	155.03	57.63	-1.19	10.1	-0.9	3.4	-134.0	-24.7	42.4	369.9
1376562551949814912	153310184	60.97	50.43	-0.97	7.9	-0.6	0.9	237.6	-65.7	-39.7	366.5
578849205092501632	207312070	227.14	32.32	-1.36	11.2	3.2	2.8	16.2	-27.6	-6.7	360.9
828352101654416640	442015248	161.53	49.31	-1.39	11.6	-1.1	4.2	-24.2	-37.2	1.5	460.0
3398415211089085440	258013114	189.27	-4.67	-0.99	11.8	0.6	-0.3	-78.7	-36.2	12.6	381.8
3072883525005327488	196812249	227.04	20.11	-1.09	11.5	3.6	1.8	-59.7	-46.0	16.2	316.7
1309070576867596032	229601019	52.09	33.68	-1.34	6.3	-2.4	2.1	185.0	-114.0	-93.8	271.5
1015712868757539712	327109055	169.84	41.52	-0.80	12.4	-0.8	3.8	-11.6	-24.7	7.0	316.0
3969220556612007168	331210090	232.65	60.73	-0.80	9.3	1.4	3.2	-153.8	-75.2	63.5	479.8
375106436290960384	7013119	123.48	-21.25	-0.66	10.4	-3.3	-1.5	-139.9	4.6	-5.5	416.2
1544386131299665024	315612213	129.50	67.46	-0.61	9.0	-1.0	3.1	-167.6	-15.7	33.0	303.7
4009546245072890368	299710019	211.31	82.49	-1.25	8.3	0.1	1.2	209.8	-29.5	-15.5	261.8
3090248799337115648	21206245	221.57	21.10	-0.66	11.4	2.8	1.7	-40.5	-44.2	2.2	389.0

TABLE 4 GL-4, 75 stars

source-id	obsid	l	b	[Fe/H]	x	y	z	U	V	W	L_c
		(deg)	(deg)	(dex)	(kpc)	(kpc)	(kpc)	(km s ⁻¹)	(km s ⁻¹)	(km s ⁻¹)	(km s ⁻¹ kpc)
3862691074020171392	215114081	238.39	51.44	-1.14	8.5	0.5	0.7	-64.8	-100.7	21.2	824.5
3983060556147457920	341205081	225.63	62.22	-1.32	8.6	0.4	1.2	44.0	-100.5	9.4	884.6
3998046590396332544	219209044	204.45	70.14	-1.55	8.6	0.2	1.4	-38.3	-105.2	10.7	901.4
629560498136247680	491914225	211.52	52.11	-1.70	8.5	0.2	0.5	39.0	-122.8	-11.9	1057.0
1030072353177238656	427411139	162.95	39.15	-1.28	8.7	-0.1	0.4	3.1	-113.3	16.5	980.4
1281563304200564480	210407087	42.03	64.71	-1.39	7.8	-0.4	1.3	-61.5	-114.5	-11.6	913.0
1361967737682703744	436304069	72.93	32.18	-1.13	7.9	-0.9	0.6	117.2	-114.5	15.7	800.0
1460408456826617216	301808195	28.02	87.53	-1.36	8.1	-0.0	1.4	-53.8	-97.0	-6.7	791.9
158927310937131648	417415146	81.31	54.73	-1.27	8.1	-0.5	0.7	10.1	-109.3	24.9	883.2
4501173868500580224	448015177	40.28	21.46	-0.73	5.4	-2.4	1.5	88.4	-187.3	-38.8	807.0
23744627482731104	372308145	153.13	-10.71	-1.29	8.7	-0.3	-0.1	-66.8	-108.0	11.4	960.3
54587801677441280	406512088	167.30	-32.80	-1.44	8.6	-0.1	-0.2	-95.5	-111.5	-13.0	965.7
2051842324124265984	369807060	70.83	9.22	-1.52	7.3	-2.7	0.5	-131.2	-65.5	-20.8	831.5
2092283667462120960	574205190	64.20	14.55	-1.33	6.5	-3.6	1.1	56.3	-168.0	-7.9	883.8
2106705205566435200	457213047	74.46	17.51	-1.19	7.6	-2.2	0.8	-163.7	-62.7	20.9	837.7
2550420510295875712	250203025	118.62	-60.13	-1.40	8.4	-0.3	-0.7	-112.1	-105.9	12.4	927.2
2567974041634213760	473508208	149.06	-52.56	-1.54	8.9	-0.4	-1.0	78.3	-99.5	24.9	850.8
2758035174935654784	361515200	94.37	-51.00	-1.37	8.3	-0.7	-0.8	-72.2	-106.0	-28.1	922.7
2828778027944351488	363008015	85.46	-37.52	-1.39	8.0	-2.6	-2.0	36.9	-111.3	9.1	792.8
2864023182410285824	284614066	115.54	-28.48	-1.65	8.6	-0.9	-0.5	-12.2	-94.6	-8.3	825.5
2864505043382651136	164509075	103.03	-34.32	-1.37	8.7	-2.0	-1.4	-16.3	-87.5	4.1	791.1
3381170883031960192	401003217	191.03	9.95	-1.26	8.7	0.1	0.1	-44.9	-108.1	18.0	937.9
397548396328513024	182713017	128.26	-18.33	-1.37	8.3	-0.1	-0.0	105.3	-115.3	-4.0	943.2
3674143933870596352	339608084	349.10	62.97	-1.82	7.9	0.0	0.5	127.2	-112.4	-32.0	899.2
3701146668138963840	435612027	281.27	63.51	-1.05	8.1	0.3	0.7	114.1	-102.2	7.4	866.7
3701052316297428992	94114192	283.66	63.96	-1.15	8.1	0.6	1.3	-33.4	-117.2	24.5	924.9
381989677659791104	83407024	244.34	33.49	-1.64	8.8	1.2	0.9	37.5	-109.4	-2.7	1003.4
383947787529667904	408915165	236.23	34.94	-1.37	8.5	0.5	0.5	65.2	-93.9	-16.7	835.4
3867919664127132928	531306171	240.03	58.23	-1.19	8.4	0.3	0.6	30.0	-123.9	11.4	1044.9
3945839785445446784	202016139	274.01	78.04	-1.46	8.2	0.1	0.4	-7.6	-115.9	14.9	949.3
3957868545732319360	334509203	293.47	87.45	-0.92	8.2	0.0	1.2	-86.5	-111.0	-2.1	903.8

3983648794868003456	215807088	227.66	63.96	-1.49	8.3	0.2	0.5	80.9	-98.6	27.5	836.3
4011197333580540416	153508020	152.79	86.86	-1.31	8.3	-0.0	1.6	78.2	-105.3	-31.1	868.7
4013781873100372992	508012079	187.43	81.20	-1.53	8.3	0.0	0.9	28.0	-125.5	-24.2	1046.9
4028191728896688128	399112211	180.33	76.66	-1.36	8.5	0.0	1.1	34.9	-114.3	2.0	967.7
4029890852318475392	556204185	171.58	76.86	-1.43	8.3	-0.0	0.5	-51.1	-109.6	20.1	912.2
95253441093777408	378502232	140.92	-41.85	-1.19	8.7	-0.4	-0.5	-48.2	-110.9	-26.9	980.6
15665777248819968	368607203	169.27	-38.46	-2.25	9.3	-0.2	-0.8	16.4	-107.1	20.7	987.3
67648113035532032	215006143	201.11	28.03	-1.43	8.6	0.2	0.3	12.6	-106.9	-24.4	921.2
723727415582400768	523308121	210.91	61.52	-1.18	8.6	0.2	0.8	57.1	-87.6	-31.0	763.9
788860014820041216	563004050	155.21	63.94	-0.93	8.6	-0.2	0.9	-42.8	-101.9	14.9	882.8
893434119048333184	226714179	185.56	21.97	0.23	8.4	0.0	0.1	-21.1	-110.2	-7.4	929.3
933175245278987520	339206053	170.83	30.58	-1.05	8.7	-0.1	0.3	-68.0	-96.1	-3.8	838.4
1284876441972634752	207004216	46.36	69.89	-1.54	7.8	-0.4	1.7	102.2	-116.2	-30.0	861.2
1358501252397563136	150401057	69.70	37.55	-1.43	7.6	-1.5	1.3	48.1	-144.3	-9.7	1026.2
1377857192531501952	458402167	64.13	52.35	-1.26	7.9	-0.6	0.8	-101.6	-105.6	7.8	894.3
1382300215940599296	576315040	68.86	44.09	-1.31	7.9	-0.9	0.9	-64.5	-101.1	8.4	851.7
1387001173609203584	433902063	73.89	45.61	-1.38	7.6	-2.0	2.1	-82.8	-82.8	17.9	794.2
1403723684611249536	437204196	79.83	47.74	-1.42	8.1	-0.6	0.7	-67.2	-123.3	-21.3	1038.9
1457430567021692416	546609055	57.84	76.38	-1.29	8.1	-0.2	0.9	55.8	-106.2	-29.6	848.9
1461674063428369920	44106194	49.20	82.96	-1.40	8.2	-0.0	0.2	-8.8	-110.9	-10.2	908.1
1477755554856192896	567811131	51.59	69.83	-1.37	8.1	-0.1	0.4	82.5	-132.7	-19.2	1067.6
1491879194032720512	455609065	75.59	66.74	-1.30	8.1	-0.4	1.1	-5.2	-132.3	-21.8	1072.7
1545676545638836096	448503076	139.33	67.71	-1.92	8.5	-0.3	1.1	59.1	-101.6	17.5	849.6
1578299639743871488	438711142	125.82	57.86	-1.35	8.4	-0.3	0.6	-112.4	-109.6	-3.1	959.5
1589188687509570048	417416161	82.65	55.68	-1.48	8.2	-0.2	0.4	-119.3	-105.1	15.8	885.4
1795085983706056960	162916207	78.54	-23.52	-1.12	8.0	-1.0	-0.4	-59.2	-110.0	-26.1	938.8
1215531068242641408	239005015	34.69	55.58	-0.83	7.6	-0.4	1.1	45.8	-134.8	-29.5	1001.1
747669354292137472	446515198	198.26	58.59	-2.24	9.0	0.3	1.4	29.9	-92.9	20.6	842.4
4010300132092253440	450616195	196.27	82.73	-0.92	8.4	0.0	1.3	4.3	-112.0	2.3	935.9
105468733044869888	173205016	143.56	-33.87	-1.29	8.6	-0.3	-0.3	-6.2	-115.6	-15.7	994.1
647812945207911040	19104199	200.23	47.07	-1.23	8.6	0.1	0.5	28.4	-97.1	-26.2	838.5
2131873984499709312	249214199	78.90	19.75	-1.30	7.3	-4.7	1.8	-50.7	-94.4	10.5	926.1
298802390907012992	267312041	137.82	-33.54	-1.51	8.7	-0.5	-0.4	2.4	-114.8	14.5	1000.6
3727921215088631296	228311012	346.20	69.52	-1.54	7.7	0.1	1.4	75.4	-112.8	7.2	876.4
3985817787712703872	106004185	223.11	58.70	-1.40	8.6	0.4	1.0	64.3	-91.9	-10.2	817.9
1264626667604880896	435811144	36.27	59.49	-1.43	7.6	-0.4	1.2	-124.1	-112.3	19.0	908.6
2864663682294138496	359806154	101.46	-33.63	-1.48	8.6	-2.1	-1.4	-84.6	-72.4	13.7	805.3
736762125930364032	505504085	196.24	63.74	-1.25	8.8	0.2	1.4	93.1	-95.2	-8.8	859.4
888198313397015552	134516227	186.50	15.43	0.00	9.4	0.1	0.3	2.1	-98.9	10.6	925.5
2051627129085490944	369807223	70.38	8.78	-1.62	6.1	-6.0	1.0	-120.6	-28.8	22.1	898.4
152206363577101568	419909082	131.20	76.34	-1.22	8.4	-0.2	1.2	-68.3	-113.1	6.8	962.6
4010006631207125504	299815052	201.38	83.49	-1.32	8.3	0.0	0.9	59.3	-104.9	-13.1	871.5
832771073246198016	385716075	158.71	59.47	-1.08	8.3	-0.1	0.3	96.9	-101.8	25.6	843.5
3892473201883627648	457705242	271.78	61.90	-1.37	8.2	0.4	0.8	-17.7	-105.2	25.9	854.2